TU Delft

Delft University of Technology

Document Version
Final published version

Licence
Dutch Copyright Act (Article 25fa)

Citation (APA)
Hoefnagel, K. N., Pedo, A. S., Casalino, D., Hulshoff, S. J., & de Prenter, F. (2026). Cyclorotor Noise Characterization Using High-Fidelity Aeroacoustic Simulations. In *32nd AIAA/CEAS Aeroacoustics Conference (2026)* Article AIAA 2026-3447 https://doi.org/10.2514/6.2026-3447

Important note
To cite this publication, please use the final published version (if applicable).
Please check the document version above.

Copyright
In case the licence states “Dutch Copyright Act (Article 25fa)”, this publication was made available Green Open Access via the TU Delft Institutional Repository pursuant to Dutch Copyright Act (Article 25fa, the Taverne amendment). This provision does not affect copyright ownership.
Unless copyright is transferred by contract or statute, it remains with the copyright holder.

Sharing and reuse
Other than for strictly personal use, it is not permitted to download, forward or distribute the text or part of it, without the consent of the author(s) and/or copyright holder(s), unless the work is under an open content license such as Creative Commons.

Takedown policy
Please contact us and provide details if you believe this document breaches copyrights.
We will remove access to the work immediately and investigate your claim.

This work is downloaded from Delft University of Technology.

Aeroacoustics Conferences
26-29 May 2026, Brussels, Belgium
32nd AIAA/CEAS Aeroacoustics Conference (2026)

10.2514/6.2026-3447

Check for updates

Cyclorotor noise characterization using high-fidelity aeroacoustic simulations

Kaj Hoefnagel* and Augustin Pedo† and Damiano Casalino‡ and Steven Hulshoff§ and Frits de Prenter¶
Delft University of Technology, Department of Flow Physics and Technology, 2629HS Delft, Netherlands

Cyclorotors are a unique propulsion type offering rapid, 360° thrust vectoring, which is especially attractive for urban air mobility (UAM) applications. For UAM, noise is a key consideration. However, there is currently little research into cyclorotor noise. This study presents the first high-fidelity aeroacoustic simulations of cyclorotors, using the lattice Boltzmann method with very large eddy simulation (LBM-VLES). A detailed investigation of the noise-generating mechanisms is conducted. Furthermore, a comparison is made with a conventional propeller of equivalent dimensions that provides the same thrust. The results show that cyclorotor noise is dominated by unsteady loading associated with blade-vortex interactions, which offsets the acoustic benefit of the lower blade velocity. In our results, the cyclorotor is not inherently quieter than a conventional propeller operating at similar thrust under isolated conditions.

Downloaded by Technische Universiteit Delft on June 5, 2026 | http://arc.aiaa.org | DOI: 10.2514/6.2026-3447

I. Introduction

The cyclorotor is a unique type of propulsion system, in which the spanwise axis of the blades is parallel to the rotation axis, see Fig. 1. In order to generate a resultant thrust force, the blades are pitched cyclically. The magnitude and phase of this pitching motion can be altered rapidly, enabling 360-degree thrust vectoring. Cyclorotors have been used for precision maritime applications, such as tugboats, for over 100 years, where they are known as Voith-Schneider propellers [1]. Recently, cyclorotors have also gained interest for applications in urban air mobility, where high maneuverability is required for vertical take-off and landing in dense urban environments [2].

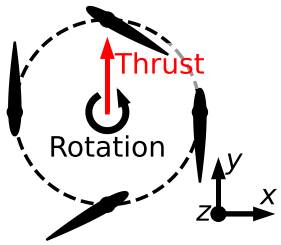

Fig. 1 Cyclorotor schematic

In urban air mobility, noise is a key consideration, as excessive noise may hinder public acceptance or certification. It is often hypothesized that cyclorotors produce less noise compared to conventional propellers, since they operate at lower rotational velocities. This results in lower blade Mach numbers, which are strongly correlated with aeroacoustic noise generation [3, 4]. However, cyclorotors also experience periodic blade loading as well as complex blade-wake interactions, both of which can increase the noise levels. To date, the only aeroacoustic study of cyclorotors is that of Halder et al. [4], who coupled a reduced order model with an acoustic solver. Although their framework was validated experimentally, it did not resolve the underlying flowfield. This meant that several important noise-generation mechanisms (such as blade-vortex interactions) were not captured. The present work addresses this limitation through high-fidelity CFD simulations of a cyclorotor using the lattice Boltzmann method with very large eddy simulation (LBM-VLES), implemented in PowerFLOW 2022-R3 with the low Mach number solver. The objectives of this work are to **1)** identify the main noise generating mechanisms of a cyclorotor and **2)** perform a quantitative noise comparison between a cyclorotor and a conventional propeller.

*PhD Candidate, Delft University of Technology, Faculty of Aerospace engineering, Department of Flow Physics and Technology, k.n.hoefnagel@tudelft.nl
†PhD Candidate, Delft University of Technology, Faculty of Aerospace engineering, Department of Flow Physics and Technology
‡Full Professor, Delft University of Technology, Faculty of Aerospace engineering, Department of Flow Physics and Technology, d.casalino@tudelft.nl
§Associate Professor, Delft University of Technology, Faculty of Aerospace engineering, Department of Flow Physics and Technology, s.j.hulshoff@tudelft.nl
¶Assistant Professor, Delft University of Technology, Faculty of Aerospace engineering, Department of Flow Physics and Technology, f.dePrenter@tudelft.nl

Copyright © 2026 by Delft University of Technology; K.
N. Hoefnagel; A.S. Pedo; D. Casalino; S.J. Hulshoff; F. de Prenter. Published by the American Institute of Aeronautics and Astronautics, Inc., with permission.

Table 1 Summary of the computational meshes used for the cyclorotor simulations.

Mesh	Finest cell size ($\Delta x/c$)	Number of cells	mean y^+ at 500 RPM	mean y^+ at 1480 RPM
2× Coarser	0.01	25×10^6	50	-
Baseline	0.005	105×10^6	28	79
1.5× Finer	0.0033	301×10^6	-	53
2× Finer	0.0025	664×10^6	15	40

The remainder of this paper is organized as follows. Section II describes the numerical methodology, including the high-fidelity LBM-VLES simulation of the cyclorotor, the considered operating conditions, verification and validation, and a BEMT model for the reference conventional propeller. Section III presents the results, including a detailed analysis of the cyclorotor noise-generating mechanisms and a comparison with the conventional propeller. Finally, Section IV summarizes the main conclusions.

Downloaded by Technische Universiteit Delft on June 5, 2026 | http://arc.aiaa.org | DOI: 10.2514/6.2026-3447

II. Methodology

Our methodology is structured as follows. Section II.A describes the numerical method underlying the high-fidelity aeroacoustic simulations of the cyclorotor. The geometry and operating conditions of both the cyclorotor and the reference propeller are then introduced in Section II.B. The cyclorotor is simulated at two operating conditions. Verification and validation of the first condition, for which experimental validation data are available, are presented in Section II.C. Verification of the second condition is described in Section II.D. Finally, Section II.E presents and validates the BEMT and acoustic model used to obtain acoustic predictions for the reference propeller.

A. Numerical method cyclorotor simulations

The high-fidelity/scale-resolved simulations are performed using the commercial CFD solver SIMULIA PowerFLOW version 6-2022-R3, which is based on the lattice-Boltzmann method (LBM). Specifically, PowerFLOW's low Mach number solver is employed, which is physically equivalent the weakly-compressible Navier-Stokes equations [5, p. 54]. PowerFLOW is based on the very large eddy simulation (VLES) methodology, where only the largest eddies are resolved and the effect of the smaller eddies is modeled using a proprietary extension of the RNG $k-\epsilon$ model [6]. Moreover, a wall model is used to represent the near-wall shear stresses without resolving the viscous sublayer. Rotational motion is simulated using sliding meshes, as described by Li [7]. Many of PowerFLOW's physical models are proprietary but derived from well-established formulations, and the solver has been extensively validated for propeller aeroacoustic simulations [8–14] and employed for UAM full-vehicle aeroacoustic studies [15–17].

The LBM employs a Cartesian mesh, which is isotropically refined using PowerFLOW's variable resolution (VR) system, where subsequent VR regions refine by a factor two. The domain of the present simulations has dimensions 35.5 m×35.5 m (280 chord lengths), within which nine VR regions are used (Figs. 2 and 3). A sponge zone is applied to all regions outside $10R$ (VR1-3) to damp outgoing acoustic waves. Between $10R$ and $17.3R$, the grid (bulk) viscosity is exponentially increased from (in lattice units) 0.005 to 0.5, and remains at this level in the outer domain. This corresponds to a dimensional bulk viscosity range of approximately $0.07\text{m}^2/\text{s}$ to $28.1\text{m}^2/\text{s}$ for the baseline mesh. The sponge zone primarily dissipates waves with less than 100 cells per wavelength. This corresponds to a cutoff frequency of approximately 21Hz for the baseline mesh, below which waves are not significantly damped.

A ring-like refinement (VR7) is used in the rotor to properly capture shed vortices impinging on following blades. Capturing this mechanism is critical for obtaining the correct aerodynamic forces. An overview of the different mesh resolutions used in this study is provided in Tab. 1, including the finest cell size, number of cells, and the surface-averaged y^+ at different operating conditions.

The motion of the cyclorotor is simulated using sliding meshes, defined with PowerFLOW's local rotating frames (LRFs). The LRFs are shown as dashed lines in Fig. 2. The outer LRF rotates with the rotor's angular velocity. The four inner LRFs are prescribed a sinusoidal angular velocity, corresponding to the pitching motion of each blade.

In order to obtain pressure in the far-field (from which noise is computed), the Ffowcs Williams-Hawkings (FW-H) acoustic analogy is used [18]. Both permeable and solid formulations are used. For the permeable formulation, pressure is recorded on three spheres with radii $2.4R$, $2.6R$, and $2.8R$. We use the FW-H implemented in SIMULIA PowerACOUSTICS to obtain the corresponding pressure in the far-field. Results of the three spheres are then averaged

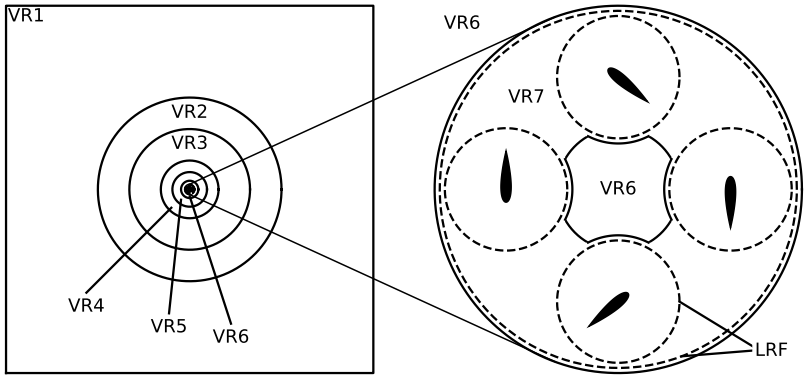

Fig. 2 Virtual refinement (VR) regions 1-7 of the cyclorotor mesh.

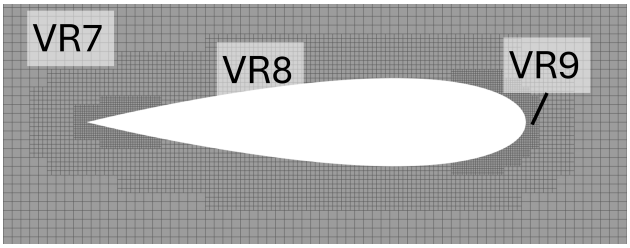

Fig. 3 Virtual refinement (VR) regions 7-9 and mesh cells near the blade.

Downloaded by Technische Universiteit Delft on June 5, 2026 | http://arc.aiaa.org | DOI: 10.2514/6.2026-3447

to filter out hydrodynamic fluctuations [19]. For the solid formulation, pressure is recorded on the surface of the blades. We then use the solid FW-H implemented in SIMULIA *Opty∂B*-PFNOISESCAN [10] to obtain pressure in the far-field. Acoustic spectra are computed over 8 rotor cycles, after discarding the first 2 cycles to ensure statistical convergence. For verification cases on finer meshes, shorter time signals (5 or 6 cycles in total) are used to limit computational cost.

B. Geometry and operating conditions

The geometry and simulated operating conditions of both the cyclorotor and the reference conventional propeller are described in this section.

1. Cyclorotor

For the cyclorotor, we use the same geometry as Halder et al. [4]: a four-bladed cyclorotor with a radius of 11 inches (0.28 m), blades with the NACA0020 profile with a chord length of 5 inches (0.13 m) and a span of 22 inches (0.56 m). Halder et al. report experimental measurements of forces and noise spectra for this configuration, which allows us to validate it.

In the experiment, the blades are pitched using a four-bar mechanism (see [20, Fig. 10]). Since the lengths of the bars are not known, we approximate the pitch cycle using a simple sine, which is relatively close (see [20, Fig. 11]). Next, Halder et al. use an aeroelastic model to predict the aerodynamic loads, from which we infer that the aeroelastic deflections of the blades are non-negligible. However, aeroelastic modeling is currently not supported in PowerFLOW, so we must neglect these effects and thus assume rigid-blade motion.

The cyclorotor is simulated at three operating conditions:

- **C1**: $V_\infty = 0$ m/s, $\theta_{\max} = 40°$, $\Omega = 500$ RPM.
- **C2**: $V_\infty = 0$ m/s, $\theta_{\max} = 35°$, $\Omega = 531$ RPM.
- **C3**: $V_\infty = 0$ m/s, $\theta_{\max} = 40°$, $\Omega = 1480$ RPM.

Here V_∞ denotes the freestream velocity, $\theta_{\max}$ is the maximum blade pitch angle, and Ω is the rotational speed.

Conditions C1 and C2 are used for validation against the experimental data of Halder et al. [4]. For C1, the predicted

forces are verified through a mesh convergence study and validated against experiments. The acoustic predictions are verified for C1 by comparing different FW-H formulations and mesh resolutions. Condition C2 is used for acoustic validation against experiments.

The third operating condition C3 is introduced for two reasons. Firstly, the disk loading of the first two operating conditions (approximately 80 N/m^2) is significantly lower than that of typical cyclorotors. For comparison, the commercial CR-60 cyclorotor*, which has similar dimensions, runs at 2600RPM and has a disk loading of about 2500N/m^2. Secondly, we want to use this operating condition to compare to the conventional propeller that is described in Section II.B.2. For C3, zero inflow velocity (hover) is again used, since it combines maximum rotor loading with close proximity to ground observers and is therefore acoustically critical. Next, the maximum blade pitch is set to $\theta_{\max} = 40°$. We base this choice on the figure presented in the study by Benedict et al. [21, Fig. 9], which shows that for thicker blades, $\theta_{\max} = 40°$ achieves the highest efficiency. Finally, the rotation rate is adjusted to match the cyclorotor thrust with the design thrust of the conventional propeller. This results in an RPM of 1480.

2. Conventional propeller

A key objective of this work is to perform a quantitative aeroacoustic comparison between a cyclorotor and a conventional propeller. To this end, a reference propeller was selected. Since these are fundamentally different propulsive devices, making a fair comparison is challenging. We choose to approximately match the diameter of the reference propeller with the diameter and span of the cyclorotor (which are equal). This results in comparable propulsion-system dimensions when mounted on a vehicle.

Since cyclorotors can operate at relatively high disk loading, we seek a propeller with high disk loading and for which the blade geometry is publicly available. The X-57 Maxwell high-lift propeller meets these requirements [22]. In addition, low noise emissions were a design objective for this propeller, suggesting relatively high aeroacoustic efficiency.

The propeller has a diameter of 0.58 m, compared to 0.56 m for the cyclorotor, and a disk area of 0.26m^2 compared to 0.31m^2 for the cyclorotor (defined as span × diameter). At its design rotational speed of 4549 RPM, the propeller produces 220 N of thrust, corresponding to a disk loading of 845N/m^2.

The propeller is simulated at the following operating conditions:

- **P1**: $V_\infty = 28.7$ m/s and 4549 RPM, for validating thrust and torque predictions.
- **P2**: $V_\infty = 38.6$ m/s and 4800 RPM, for validating the acoustics.
- **P3**: $V_\infty = 0$ m/s and 4549 RPM, for the comparison to the cyclorotor.

C. Cyclorotor verification and validation at operating conditions C1 and C2

To verify and validate the numerical setup, operating conditions C1 and C2 are considered, for which experimental data from Halder et al. are available [4]. First, a mesh convergence study is presented at C1 for thrust and power, including validation against experiments. Next, the acoustic predictions are verified at C1 using different FW-H formulations and mesh resolutions. Finally, the acoustic predictions are validated at C2.

1. Thrust and power

The total thrust and power histories are presented as a sliding-window average over one rotor cycle (i.e., the value at time t represents the mean over the interval $[t - t_{\text{cycle}},\ t]$). Results for the cyclorotor at operating condition C1 (500 RPM and $\theta_{\max} = 40°$) are shown in Fig. 4 for the mesh resolutions listed in Tab. 1, together with the experimental results of Halder et al. [4].

In the first two cycles, strong initialization effects are observed, which dissipate rapidly. Up to approximately the fourth cycle, the mean slightly decreases, likely due to wake development. In subsequent cycles, the mean remains stable. For the time-converged results, a difference of approximately 2.5% is observed between the baseline and 2× finer mesh for both thrust and power. Meanwhile, the 2× coarser mesh has a slightly lower thrust but a significantly lower power. We believe that this behaviour can be attributed to excessive numerical dissipation on the 2× coarser mesh, which weakens the vortex shed by one blade before it impinges on the following blade, thereby reducing the induced drag and the associated power consumption.

*CycloTech GmbH, "Rotor Solutions," CycloTech, https://web.archive.org/web/20260215015641/https://www.cyclotech.aero/rotor-solutions, accessed 2 March 2026.

Downloaded by Technische Universiteit Delft on June 5, 2026 | http://arc.aiaa.org | DOI: 10.2514/6.2026-3447

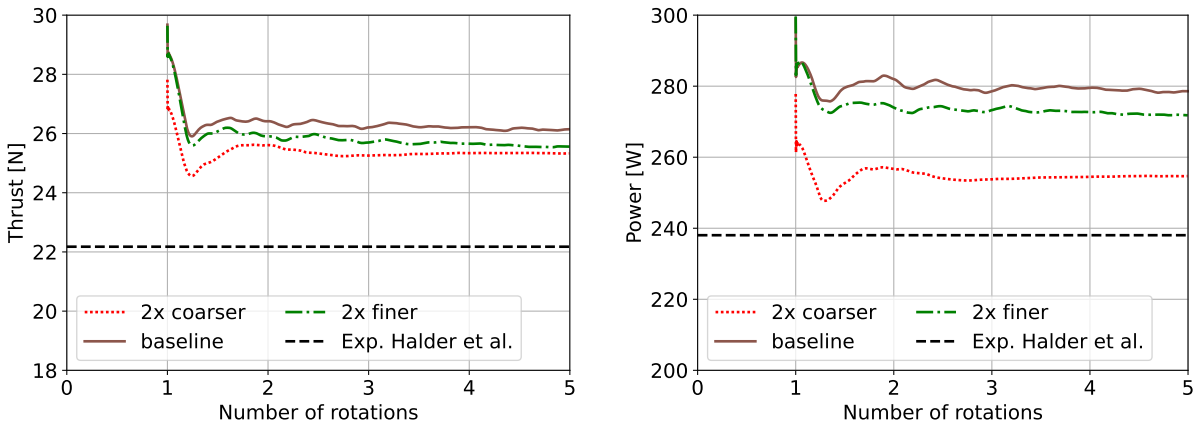

Fig. 4 Sliding-window averaged thrust and power through time for three mesh resolutions, for operating condition C1 (500 RPM and 40° maximum pitch angle). Experimental results from Halder et al. [4] are added for validation.

The simulated thrust and power are approximately 18% higher than the experimental results of Halder et al. This discrepancy is attributed to the two physical differences between their setup and our simulation discussed before. Firstly, we prescribe a sinusoidal pitching function, whereas their four-bar mechanism generates a slightly non-sinusoidal motion (see [20, Fig. 11]). In particular, their blades spend less time at the most negative pitch angles, where the lift and drag forces are largest. Secondly, we model the blades as rigid, while the experimental blades experienced significant aeroelastic deformation. This deformation effectively reduces the angle of attack, thereby decreasing lift and drag. The reduced lift and drag on the blades may lead to the lower total thrust and power observed.

2. Aeroacoustic noise

The first step is to verify the ability of the FW-H formulation to reproduce acoustic signals at arbitrary observer locations. To this end, a probe is placed in the computational domain, at an upstream location with coordinates $(x, y, z) = (0.13\text{m}, 1.25\text{m}, 0\text{m})$ to prevent contamination by hydrodynamic fluctuations. The 1/12-octave spectrum obtained from this probe is compared with the spectra predicted by the solid and permeable FW-H formulations, as shown in Fig. 5a. Both FW-H formulations accurately predict the peaks at the first and second blade passing frequencies (BPFs), at 33 and 67Hz, respectively. For the broadband noise ($\geq$ 100Hz), deviations are observed between FW-H predictions and the probe signal. A significant peak is also observed in all signals at half the BPF (17Hz), indicating a possible inhomogeneity between different blades. Such behaviour has previously been observed in PowerFLOW when blades have different orientations with respect to the Cartesian mesh [23]. This effect is attributed to slight anisotropy in the boundary treatment, as shown by Li [7, Fig. 4.5]. If this peak is indeed a discretization artefact, it is expected to decrease with mesh refinement, which is investigated next.

At the same location, spectra obtained using the solid FW-H formulation on both the baseline and the 2× finer mesh are shown in Fig. 5b, together with the direct probe result from the 2× finer mesh. For consistency, spectra for both meshes are computed over the last three cycles. The peak at half the BPF (17 Hz) almost completely disappears on the 2× finer mesh, confirming that it is a discretization artefact. At the first BPF, meshes show good agreement (within 1 dB). At the second BPF, the baseline mesh deviates by approximately 4 dB. For the broadband noise ($\geq$ 100Hz), deviations are again observed between the FW-H prediction and the probe signal.

In the present study, we focus on the first BPF as it is the dominant source of noise. Hence, the baseline mesh is used for the 500 RPM cases in the remainder of this study. Furthermore, we use the solid FW-H since it closely matches the permeable FW-H, but allows a more detailed noise characterization, specifically the distinction between thickness and loading noise.

For validation of the acoustic predictions, experimental data from Halder et al. [4] are used. They report 1/3-octave spectra at various RPMs for a microphone located at a distance of $7R$ (77 inches, 1.96 m) from the rotor center. We estimate this microphone to be positioned at an angle of 45° with respect to the horizontal axis, corresponding to the

Downloaded by Technische Universiteit Delft on June 5, 2026 | http://arc.aiaa.org | DOI: 10.2514/6.2026-3447

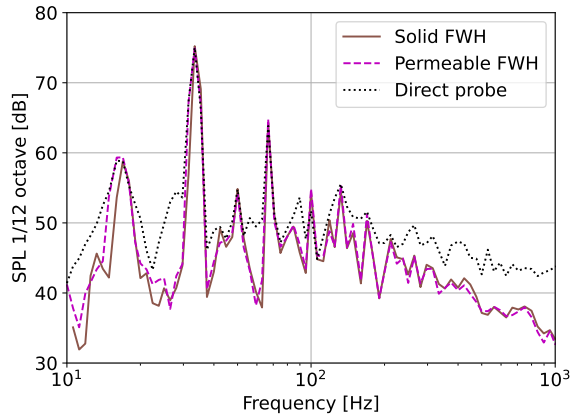

(a) Comparison between 1) solid FW-H formulation in *Opty∂B*-PFNOISESCAN, 2) permeable FW-H formulation in PowerACOUSTICS, and 3) a direct probe. All on the baseline mesh.

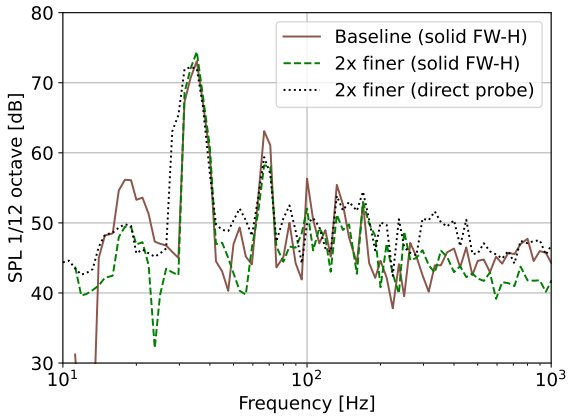

(b) Comparison between 1) solid FW-H on the baseline mesh, 2) solid FW-H on the 2× finer mesh, and 3) a direct probe in the 2× finer mesh. Averaging is performed over the last 3 cycles.

Fig. 5 1/12-Octave spectra at location $(x, y, z) = (0.13\text{m}, 1.25\text{m}, 0\text{m})$, for operating condition C1 (500 RPM and 40° maximum pitch angle).

location $(x, y, z) = (1.38\text{m}, -1.38\text{m}, 0)$. As Halder et al. report the microphone to be positioned 0.25 inch above the concrete surface, ground reflections are modeled using a reflection plane in *Opty∂B*-PFNOISESCAN. A simulation is run at the same conditions (531 RPM, 35° maximum pitch angle) and the solid FW-H is used to obtain the spectrum at the same location, the spectra are shown in Fig. 6. The noise at the first BPF (corresponding to 35Hz) is slightly overpredicted. This is to be expected, as the blade forces were also overpredicted. Next, broadband noise seems to be overpredicted. However, it should be noted that Halder et al. used harmonic averaging to obtain their spectra, which suppresses non-harmonic components such as broadband noise [24].

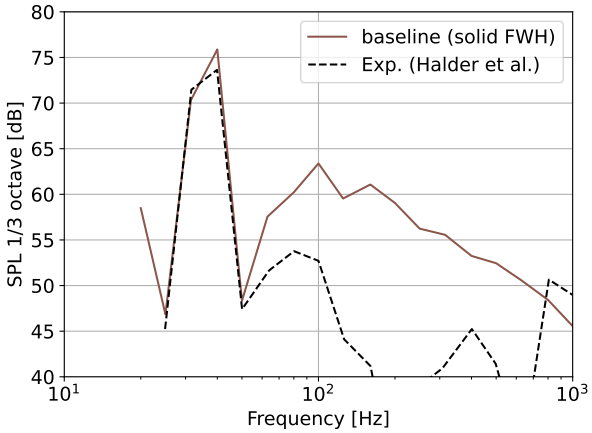

Fig. 6 1/3-Octave spectra at location $(x, y, z) = (1.38\text{m}, -1.38\text{m}, 0)$, for operating condition C2 (531 RPM and 35° maximum pitch angle). Comparing the present simulation (solid FW-H, baseline mesh) with experimental results from Halder et al. [4].

Downloaded by Technische Universiteit Delft on June 5, 2026 | http://arc.aiaa.org | DOI: 10.2514/6.2026-3447

D. Cyclorotor verification at the operating condition C3

In this section, the numerical setup is verified for operating condition C3, which is used in the subsequent results. Section II.D.1 presents a mesh convergence study for thrust and power. Section II.D.2 verifies the acoustic predictions using different FW-H formulations and mesh resolutions.

1. Thrust and power

The thrust and power histories at operating condition C3 are evaluated using the same sliding-window averaging over one rotor cycle as described previously. A mesh convergence study is performed using the baseline mesh, a 1.5× finer mesh, and a 2× finer mesh (see Tab. 1). The results are shown in Fig. 7.

Strong initialization effects are again observed during the first two cycles. In subsequent cycles, the thrust shows a slight decrease, likely due to wake development. Power, on the other hand, remains relatively stable. Thrust and power values averaged over the final cycle are taken for the following analysis. The baseline and 1.5× finer mesh yield very similar thrust values, whereas the 2× finer mesh predicts approximately 1% lower thrust. In terms of power, a slight decrease is observed with mesh refinement. However, the difference between the baseline and 2× finer mesh is only 4%, and the difference between the 1.5× and 2× finer meshes is only 2.5%.

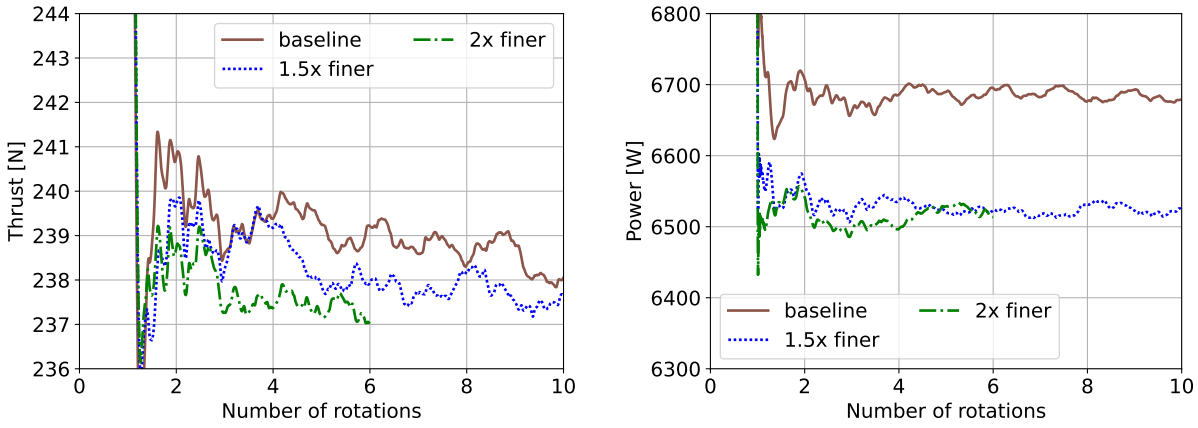

Fig. 7 Sliding-window averaged thrust and power through time for three mesh resolutions, for operating condition C3 (1480 RPM and 40° maximum pitch angle).

2. Aeroacoustic noise

The ability of the FW-H formulation to predict noise at arbitrary observer locations is now verified. First, the directivities obtained using the solid and permeable FW-H formulations are compared in Fig. 8. Both formulations show good agreement at most locations, except near the $z-$axis, which coincides with the rotation axis of the cyclorotor.

Next, the spectra predicted by both FW-H formulations are compared with a direct probe placed at the upstream location $(x, y, z) = (0.13\,\text{m}, 1.25\,\text{m}, 0\,\text{m})$. The 1/12th-octave spectra are shown in Fig. 9a. Good agreement between both formulations and the probe is observed over the range 20-1000 Hz.

Next, a mesh convergence study is performed. The baseline mesh, 1.5× finer mesh, and 2× finer mesh are compared at the location (100m, 0m, 0m), which exhibits the highest overall sound pressure level (OASPL). The corresponding 1/12-octave spectra are shown in Fig. 9b. All three meshes show good agreement at the first two BPFs. The baseline mesh underpredicts the third BPF. All meshes show small differences in the broadband range. Furthermore, the baseline mesh and 1.5× finer mesh exhibit a small peak at 1/2BPF, which is attributed to numerical artefacts as discussed previously. Since the third BPF is significant in A-weighted noise analyses, the 1.5× finer mesh is used in the subsequent analysis. The solid FW-H formulation is used for the detailed noise analysis in Section III.A, as it enables decomposition of the noise into several components. The permeable FW-H formulation is used for the comparison with the propeller.

Downloaded by Technische Universiteit Delft on June 5, 2026 | http://arc.aiaa.org | DOI: 10.2514/6.2026-3447

Downloaded by Technische Universiteit Delft on June 5, 2026 | http://arc.aiaa.org | DOI: 10.2514/6.2026-3447

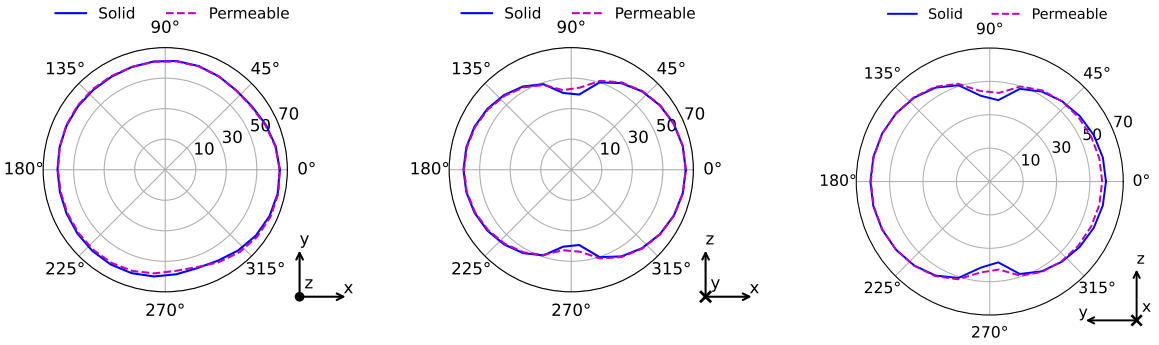

Fig. 8 OASPL directivity comparing the solid FW-H formulation in *Optyð B*-PFNOISESCAN with the permeable FW-H formulation in PowerACOUSTICS, at condition C3 (1480 RPM and 40° maximum pitch angle). Axes are defined such that thrust is in $+y$-direction and rotation around the z-axis.

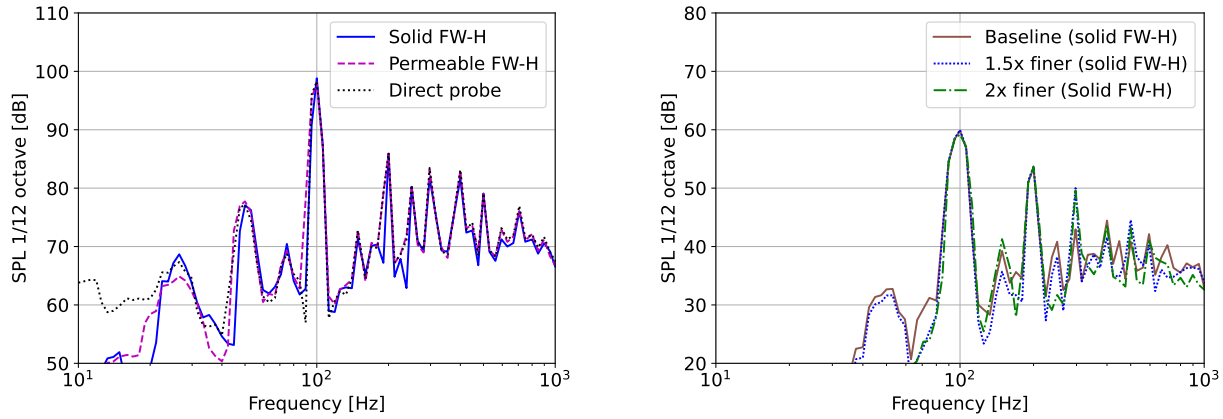

(a) Comparison between spectra from the solid FW-H formulation in *Optyð B*-PFNOISESCAN, the permeable FW-H formulation in PowerACOUSTICS, and a direct probe. All on the 1.5× finer mesh at location $(x, y, z) = (0.13\text{m}, 1.25\text{m}, 0\text{m})$.

(b) Comparison of solid FW-H at three different mesh resolutions. At location $(x, y, z) = (100\text{m}, 0\text{m}, 0\text{m})$

Fig. 9 1/12-Octave spectra at condition C3 (1480 RPM and 40° maximum pitch angle).

Downloaded by Technische Universiteit Delft on June 5, 2026 | http://arc.aiaa.org | DOI: 10.2514/6.2026-3447

E. BEMT model for conventional propeller

An original contribution of this work is the aeroacoustic comparison between a cyclorotor and a conventional propeller. To generate acoustic data for the conventional propeller, the blade element momentum theory (BEMT) model implemented in *Opty∂B*-BEMT is used to calculate the radial distribution of forces, and then there are used by the tool *Opty∂B*-PNOISE to calculate the noise by means of a compact monopole/dipole FW-H formulation [25]. Further details can be found in the work of Casalino et al. [14]. Although the BEMT model is lower fidelity than the high-fidelity simulations used for the cyclorotor, Casalino et al. showed good agreement with experiments for the tonal noise. Since tonal noise is the dominant aeroacoustic component for this propeller, this model is considered sufficient for the propeller analysis. It should be noted, however, that broadband noise is not captured, which may lead to an underprediction of noise levels in directions where broadband dominates, particularly along the rotation axis. In this section, the predicted forces and acoustic emissions are validated against experimental measurements of the X-57 propeller.

1. Thrust and torque validation

The thrust and torque are validated first. The propeller is run at condition P1 (V_∞ = 28.7 m/s and Ω = 4549 RPM), which corresponds to an advance ratio of 0.657. The thrust and torque coefficient predicted by *Opty∂B*-BEMT are shown in Tab. 2, together with experimental measurements reported by Litherland et al. [22]. Litherland et al. report measurements for two types of blades (left-handed and right-handed). Data from the left-handed blades are used here, as these blades are reported to be more stiff and thus closer to the rigid blades assumed in the BEMT model. The thrust and torque show satisfactory agreement with the experimental data, within 13% and 8%, respectively.

Table 2 Validation of *Opty∂B*-BEMT force prediction of X-57 propeller. At 4549 RPM and advance ratio 0.657.

Method	Thrust coefficient	Torque coefficient
Opty∂B-BEMT	0.266	0.0437
Experiment [22]	0.235	0.0406

2. Aeroacoustic noise validation

The acoustic predictions are validated next using experimental measurements from Litherland et al. [22]. We again use the data from their left-handed blades. Condition P2 is used (V_∞ = 38.6 m/s and Ω = 4800 RPM), for which acoustic data are available. First, consider the sound pressure level spectrum shown in Fig. 10a. The noise is dominated by the first blade passing frequency (BPF), which is predicted within 2 dB. Note that the BEMT model does not include broadband noise. However, due to the dominance of the first BPF, this is not critical for the present comparison.

Next, Litherland et al. also measured the acoustic directivity using an array of microphones positioned at a radial distance of 3.54 m from the propeller rotation axis. The microphones were placed at different observer angles relative to the propeller rotation axis, with 0° corresponding to the upstream direction. The present model was used to compute noise at the same microphone locations. The resulting directivity is shown in Fig. 10b. The BEMT model agrees well with the experiment for observer angles between 50° and 130°. For larger observer angles, the experiment shows an increase in noise, which is not captured by the present model. This increase was also not captured by the model of Litherland et al. They attribute the increase to reflections in the experiment.

III. Results

A detailed analysis of the noise-generating mechanisms of the cyclorotor is first presented in Section III.A. Next, the aeroacoustic comparison between the cyclorotor and the conventional propeller is presented in Section III.B.

A. Cyclorotor noise analysis

In the following, results from the high-fidelity simulation are used to investigate the primary mechanisms responsible for noise generation in the cyclorotor. First, the overall directivity is examined, followed by spectral characteristics, and finally the dominant source regions and mechanisms are identified. All results presented here correspond to the cyclorotor at operating condition C3 (V_∞ = 0 m/s, $\theta_{\max}$ = 40°, and Ω = 1480 RPM), using the 1.5× finer mesh.

We first analyze the overall sound pressure level (OASPL) directivity of the cyclorotor, shown in Fig. 11. This

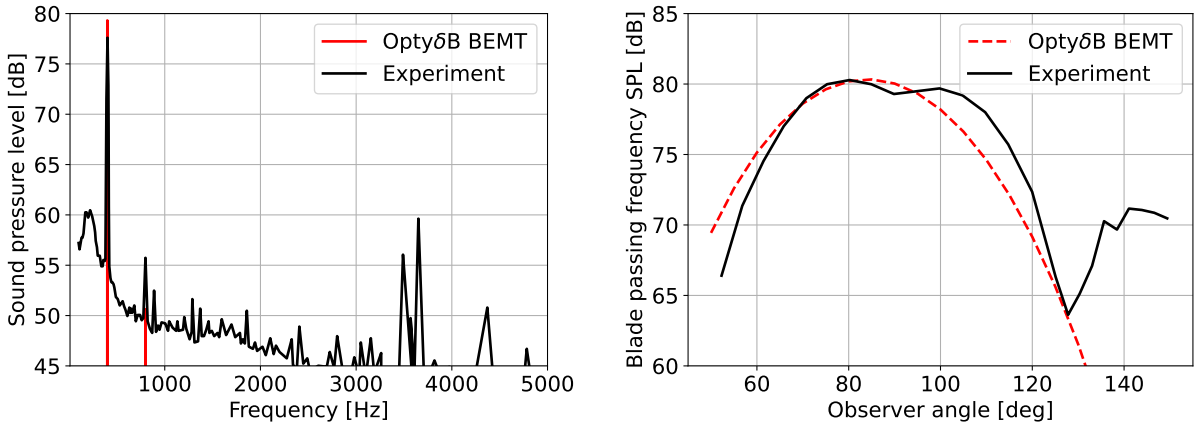

(a) Sound pressure level spectrum at observer angle 95°. **(b) Sound pressure level at blade passing frequency versus observer angle.**

Fig. 10 Validation of the noise predictions by the *Opty∂B*-BEMT BEMT model with compact FW-H formulation against experimental data by Litherland et al. [22].

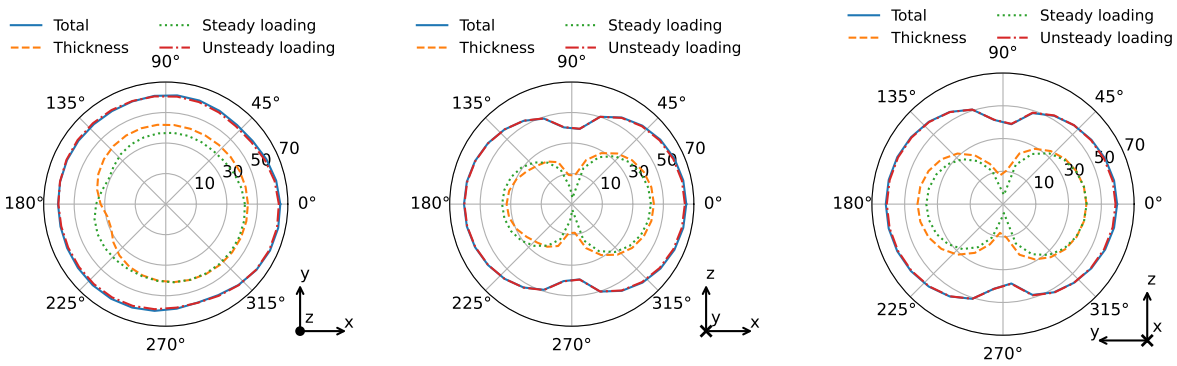

Fig. 11 OASPL directivity comparing the different components of the cyclorotor noise. Axes are defined such that thrust is in $+y$-direction and rotation around the z-axis.

directivity was obtained using the solid FW-H formulation, which allows the noise to be decomposed into thickness (monopole), steady loading (constant dipole), and unsteady loading (time-varying dipole) contributions. The results show that the cyclorotor noise is dominated by the unsteady loading component. This is expected, as the aerodynamic blade forces reverse direction every half rotation. Regarding the directivity pattern itself, the noise is relatively constant in the rotation plane (xy-plane), with a peak near 0°. In contrast, a decrease of approximately 20dB is observed near the rotation axis ($z-$axis). This behaviour can be explained by the fact that the monopoles and dipoles on the top and bottom surfaces of the blades have almost no contribution in this direction. The dipoles on the side surfaces of the blades do have a contribution, but these experience much smaller loads compared to the top and bottom surfaces.

We now examine the noise spectra at several microphone locations. The first location is $(x, y, z) = (100\text{m}, 0\text{m}, 0\text{m})$, the corresponding spectrum is shown in Fig. 12a. A tonal peak is found at the first blade passing frequency (BPF) of 100Hz for all noise components. The unsteady loading noise also exhibits clear peaks at the higher harmonics, indicating non-sinusoidal behaviour that will be investigated later in this section. The second microphone location is downstream at $(x, y, z) = (0\text{m}, -100\text{m}, 0\text{m})$, the corresponding spectrum is shown in Fig. 12b. Again, the thickness and steady loading noise only exhibit a peak at the first BPF, whereas the unsteady loading component also contains significant higher harmonics. The first harmonic is approximately 5dB lower than that at the first microphone location.

Downloaded by Technische Universiteit Delft on June 5, 2026 | http://arc.aiaa.org | DOI: 10.2514/6.2026-3447

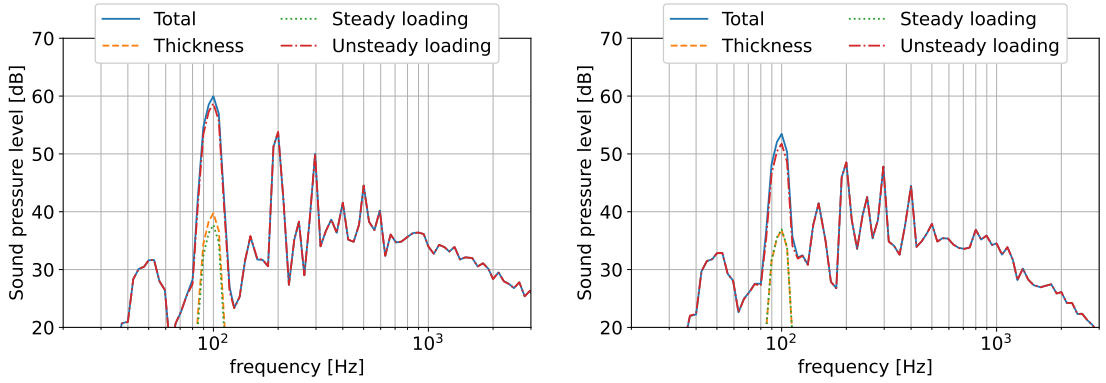

(a) Position $(x, y, z) = (100\text{m}, 0\text{m}, 0\text{m})$ **(b) Position $(x, y, z) = (0\text{m}, -100\text{m}, 0\text{m})$**

Fig. 12 1/12-Octave SPL spectra at two locations, comparing the various noise components of the cyclorotor.

Downloaded by Technische Universiteit Delft on June 5, 2026 | http://arc.aiaa.org | DOI: 10.2514/6.2026-3447

The unsteady loading noise at the first microphone location ($(x, y, z) = (100\text{m}, 0\text{m}, 0\text{m})$) is analyzed in more detail, as this location corresponds to the highest noise levels. To localize the dominant noise sources, the FW-H contributions of individual surface elements to the acoustic pressure at this microphone location are examined. Specifically, a Fourier transform is applied to the pressure signal associated with each surface element at the microphone. The sound pressure level (SPL) of the first blade passing frequency (BPF) is then extracted to construct a source map over the blade surface. The resulting source map is shown in Fig. 14. The location of maximum SPL per unit area is indicated with a red ▼.

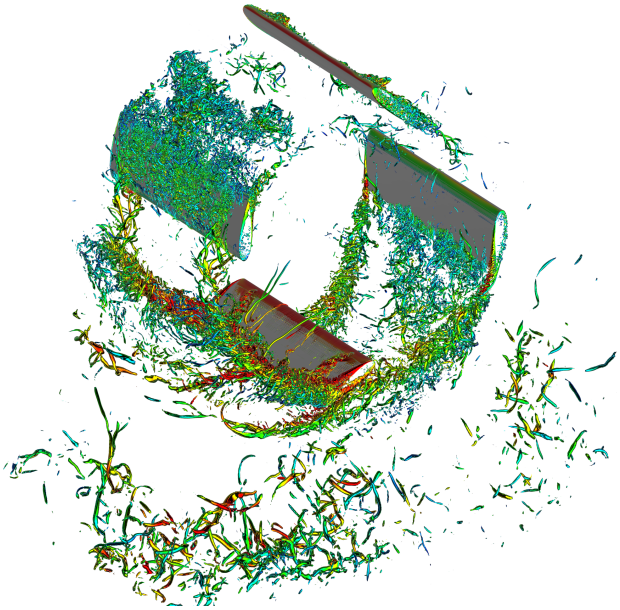

Fig. 13 Isosurfaces of $\lambda_2 = 10^7$ for the cyclorotor at condition C3 (1480 RPM and 40° maximum pitch angle), colored by velocity magnitude.

Most of the unsteady loading noise originates from the leading edge and the front portion of the inner surface, primarily near the mid-span region ($-0.3 < z/\text{span} < 0.3$). The highest BPF SPL per unit area is observed at the leading edge at $z = 0.25\text{span}$. Two aerodynamic phenomena may contribute to the strong noise generation at the leading edge. First, the leading edge vortex that forms in dynamic stall can produce strong suction peaks near the leading edge. Second, when this vortex convects downstream and impinges on the following blade, it may also create strong pressure fluctuations that contribute to the observed noise. The vortices shed during dynamic stall are also visible in the flow visualization in Fig. 13.

To further investigate the noise production at the leading edge, the acoustic pressure per unit area generated by a single surface element is examined at the microphone location (100m, 0m, 0m). The selected surface element corresponds to the location of maximum unsteady loading noise (marked with a red ▼ in Fig. 14). The resulting pressure signal is shown in Fig. 15. As before, the acoustic pressure is decomposed into thickness, steady loading, and unsteady loading contributions. Furthermore, the x-axis represents the observer time over a single rotation cycle, with several cycles overlaid to illustrate cycle-to-cycle variations. Due to acoustic propagation effects, there is no one-to-one mapping between observer time and blade azimuth. However, for the present low Mach number, $t = 0t_{\text{cycle}}$ corresponds approximately to the blade at zero pitch angle traveling downstream (the leftmost blade in Fig. 1).

First consider the unsteady loading component. Between $0t_{\text{cycle}}$ and $0.4t_{\text{cycle}}$, as well as between $0.9t_{\text{cycle}}$ and $1t_{\text{cycle}}$, significant variation between cycles is observed. In addition, large pressure peaks occur between $0.25t_{\text{cycle}}$ and $0.4t_{\text{cycle}}$, which are not repeated in other cycles. We attribute these stochastic variations and pressure peaks to blade-vortex

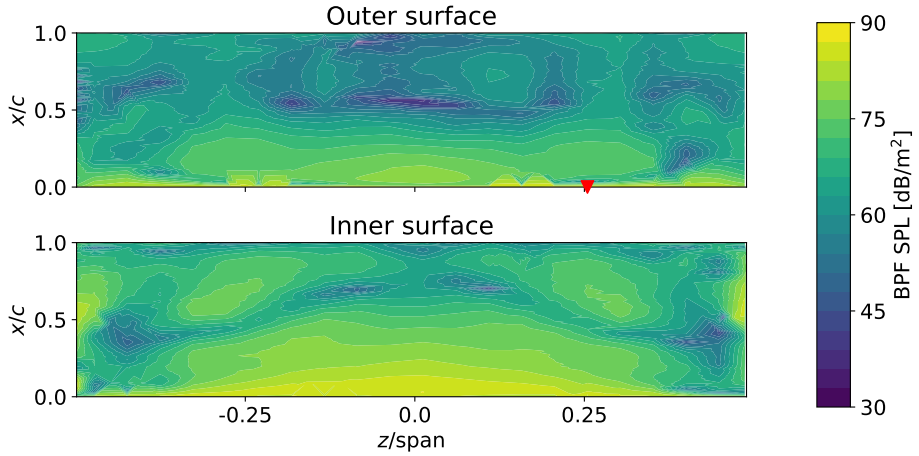

Fig. 14 Source map of the sound pressure level (SPL) of the first blade passing frequency (BPF) over the blade surface of the cyclorotor at the microphone at $(x, y, z) = (100\text{m}, 0\text{m}, 0\text{m})$. The red ▼ marks the location of maximum dB/m^2.

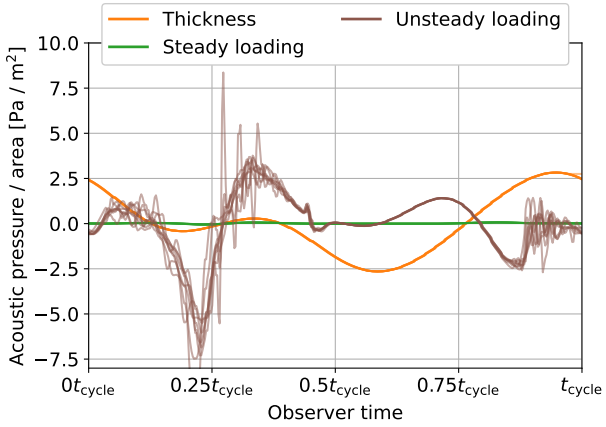

Fig. 15 Components of acoustic pressure per unit area due to a single surface element (marked with a red ▼ in Fig. 14), propagated to the observer location $(x, y, z) = (100\text{m}, 0\text{m}, 0\text{m})$.

Downloaded by Technische Universiteit Delft on June 5, 2026 | http://arc.aiaa.org | DOI: 10.2514/6.2026-3447

interaction (BVI), in which vortices coming from one blade impinge on the leading edge of the following blade. Two types of vortices may contribute to this interaction: the spanwise vortex shed during dynamic stall, and the azimuthal tip vortices generated by the blade loading. The latter are observed to convect inward and interact with the following blade.

Even if the stochastic component were absent, the unsteady loading pressure still exhibits large periodic variations, which could contribute to the noise generation. It is not yet clear whether this non-stochastic part arises from periodic blade-vortex interaction or from the periodic blade loading due to pitching. In future work, this will be investigated by running simulations with a single blade, thereby eliminating blade-vortex interactions.

Finally, consider the thickness and steady loading components. The thickness pressure signal exhibits much larger variations, comparable to those of the unsteady loading component. However, the thickness and steady loading contributions were previously found to produce similar overall noise levels, both significantly lower than the unsteady loading noise. This suggests that thickness noise from the individual blades partially cancels through destructive interference, resulting in a significantly reduced net contribution. In addition, the thickness noise signal is relatively smooth, indicating that higher harmonics are weak.

Based on the analysis above, several potential approaches for reducing cyclorotor noise can be considered. First, winglets or endcaps could be added to reduce the strength of the tip vortices and thereby mitigate blade-vortex interactions. However, the dynamic stall vortex would remain and could potentially become stronger, so the net acoustic impact is uncertain. Second, the strength of the blade-vortex interaction could be reduced by decreasing either the maximum pitch angle or the number of blades. In both cases, the rotational speed would have to be increased to maintain the same thrust, which would tend to increase noise. It is therefore unclear whether the net noise would increase or decrease.

Downloaded by Technische Universiteit Delft on June 5, 2026 | http://arc.aiaa.org | DOI: 10.2514/6.2026-3447

B. Comparison to conventional propeller

The acoustic performance of the cyclorotor is now compared with that of the conventional propeller. The propeller is operated at condition P3 (V_∞ = 0 m/s and Ω = 4549 RPM). The cyclorotor is operated at condition C3 (V_∞ = 0 m/s, $\theta_{\max} = 40°$, and 1480 RPM). This rotational speed was selected to approximately match the thrust of the propeller. The resulting thrust, power, and efficiency of both devices are reported in Tab. 3. The cyclorotor produces nearly the same thrust while requiring slightly less power.

Table 3 Thrust, power, and efficiency resulting from the cyclorotor simulation (LBM-VLES) and the propeller BEMT model.

Device	Thrust [N]	Power [kW]	Efficiency [N/W]
Cyclorotor (LBM-VLES)	238	6.53	0.036
Propeller (BEMT)	242	7.34	0.033

The directivity of the overall sound pressure level (OASPL) is shown in Fig. 16 for microphones at a radial distance of 100m. For consistency, the results are plotted such that the thrust always aligns with the +y-axis. This means that the cyclorotor rotates about the z-axis, while the propeller rotates about the y-axis. A common postprocessing step is to apply A-weighting to the acoustic signal. This weighting approximates the sensitivity of the human ear and therefore gives a more meaningful comparison in terms of perceived loudness. Concretely, A-weighting weights frequencies in the range 1-10kHz most heavily, while frequencies further away from this band are increasingly weighted less. The A-weighted directivity is also shown in Fig. 16.

The cyclorotor and propeller produce markedly different directivity patterns, partly due to their different rotation axes. Both devices produce relatively low noise levels along their respective rotation axes. This means that the propeller produces less noise (both unweighted and A-weighted) in the y-direction, while the cyclorotor produces less noise in the z-direction. For urban air mobility vehicles, noise in the y-direction (below the hovering vehicle) is usually critical, as observers there are closest to the noise source. Finally, consider the noise along the x-axis. In terms of unweighted noise, the cyclorotor is louder than the propeller. However, when A-weighting is applied, both devices produce similar noise levels.

We further investigate the nature of the noise by comparing 1/12-octave sound pressure level (SPL) spectra at two observer locations: in the rotation plane of the propeller (100m, 0m, 0m) and downstream of the propeller (0m, -100m, 0m). The corresponding spectra are shown in Fig. 17a and Fig. 17b, respectively. A-weighted spectra are also included.

In Fig. 17a, the propeller's acoustic energy is dominated by the first BPF, whereas the cyclorotor's acoustic energy is also distributed into higher harmonics. If the cyclorotor spectrum contained only the first BPF, its A-weighted noise

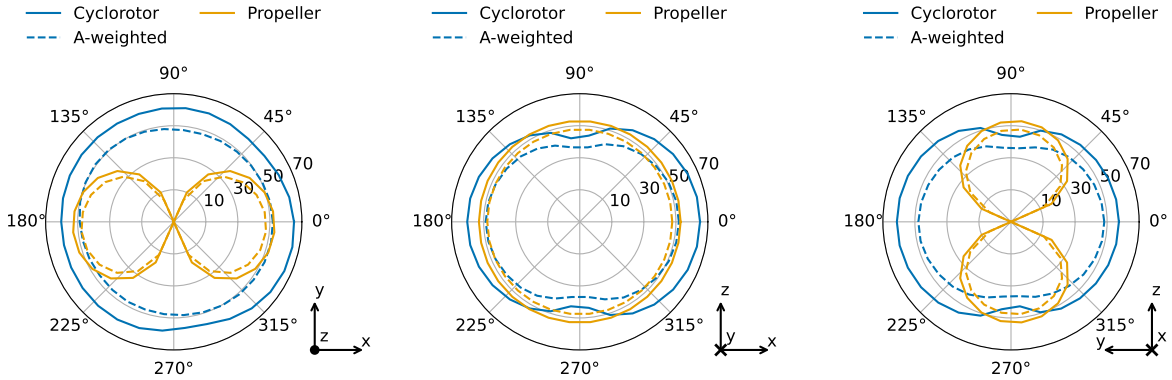

Fig. 16 OASPL directivity comparing the cyclorotor and conventional propeller. Axes are defined such that both produce thrust in $+y$-direction, the cyclorotor rotates around the z-axis and the propeller around the y-axis.

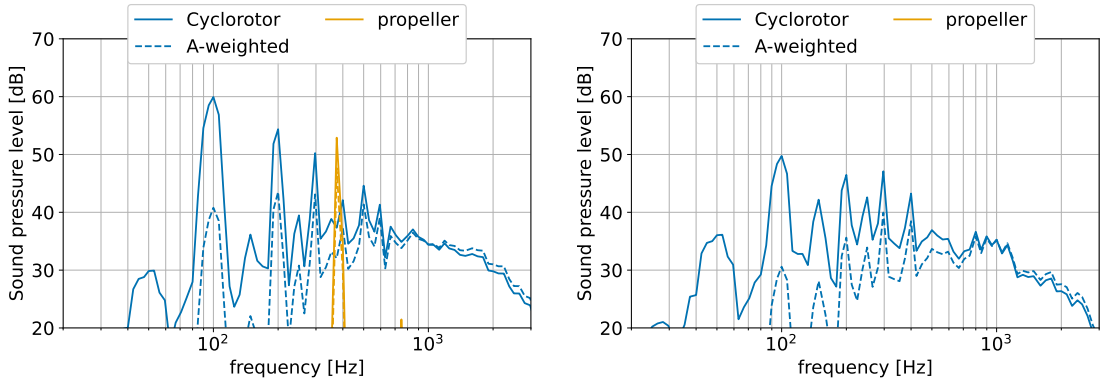

(a) Position $(x, y, z) = (100\text{m}, 0\text{m}, 0\text{m})$ **(b) Position $(x, y, z) = (0\text{m}, -100\text{m}, 0\text{m})$**

Fig. 17 1/12-Octave SPL spectra at two observer locations, comparing the cyclorotor and propeller.

would be lower than that of the propeller. However, with the higher harmonics, the cyclorotor's noise is approximately equal to that of the propeller. Still, this result demonstrates that the cyclorotor benefits more strongly from the particular sensitivity of the human ear (i.e. A-weighting) than the propeller, due to its lower rotation rate and corresponding lower BPF.

For the downstream microphone spectrum in Fig. 17b, the propeller produces no tonal noise. This is consistent with dipole radiation characteristics, which predict no noise along the rotation axis. In reality, broadband noise would still be present in this direction, but we expect this to be significantly less than the tonal component in the rotation plane.

Overall, the present comparison suggests that the cyclorotor is not inherently quieter than a conventional propeller when operated at comparable thrust. Despite its lower rotation rate, the cyclorotor produces similar A-weighted noise levels and is louder in the downward (y) direction below a hovering vehicle, which is acoustically critical for urban air mobility applications. The potential benefit of the lower blade passing frequency is largely offset by unsteady loading noise associated with blade-vortex interactions. It should be noted, however, that the cyclorotor configuration considered here was not acoustically optimized, unlike the propeller.

Another important caveat to the present analysis is the effect of installation. The cyclorotor inherently exhibits strong unsteady loading effects due to its pitching kinematics as well as blade-vortex interactions. As a result, installation effects (e.g. inflow distortion or airframe interaction) are expected to introduce relatively little additional unsteadiness. In contrast, conventional propellers typically operate under relatively steady loading in isolated conditions, which is also the case in our BEMT model. This implies that conventional propellers are more sensitive to installation effects, which may significantly increase noise levels. For example, Sinnige reports increases of up to 24 dB due to a pylon upstream

Downloaded by Technische Universiteit Delft on June 5, 2026 | http://arc.aiaa.org | DOI: 10.2514/6.2026-3447

of the propeller [26]. Furthermore, Zarri et al. studied the influence of adjacent propellers and found increases of up to 50 dB along the rotation axis compared to the isolated case [27]. This suggests that the relative acoustic performance observed here may change under installed conditions.

IV. Concluding remarks

A high-fidelity aeroacoustic simulation of a cyclorotor was performed using the lattice Boltzmann method with very large eddy simulation (LBM-VLES). The predicted aerodynamic forces were verified and validated. Far-field noise was computed using a solid Ffowcs Williams-Hawkings (FW-H) acoustic analogy, which was validated for the tonal contribution. In addition, a BEMT model combined with an acoustic analogy was used to simulate a reference conventional propeller of similar dimensions as the cyclorotor. The predicted thrust, power, and acoustics of this model were also validated.

A detailed analysis of the noise-generating mechanisms in the cyclorotor was carried out using the high-fidelity simulation data. The noise was found to be dominated by unsteady loading noise, primarily produced near the leading edge of the blades. The unsteady loading pressure at the leading edge exhibits significant cycle-to-cycle variations as well as large stochastic pressure peaks. These observations strongly suggest that blade-vortex interaction plays an important role in the noise generation in the cyclorotor.

Finally, a comparison was made between the cyclorotor and a conventional propeller (simulated using the BEMT model). Both devices had comparable dimensions and produced similar thrust in hover conditions. Markedly different directivity patterns were observed, with both devices producing significantly lower noise levels along their respective rotation axes. As a result, the cyclorotor is quieter in the lateral direction, while the propeller is quieter in the vertical direction (towards the ground in hover). In the longitudinal direction, the cyclorotor produces higher unweighted noise levels than the propeller, but similar levels when A-weighting is applied. Overall, these results suggest that the lower rotation rate of the cyclorotor does not automatically result in lower noise, and that it is not inherently quieter than a conventional propeller operating at similar thrust under isolated conditions.

References

[1] Esmailian, E., Ghassemi, H., and Heidari, S. A., "Numerical investigation of the performance of Voith Schneider propulsion," *American Journal of Marine Science*, Vol. 2, No. 3, 2014, pp. 58–62.

[2] Roshanian, J., Darvishpoor, S., Georgiev, K., and Serbezov, V., "Vehicle Configurations, Infrastructures, and Future of Urban Air Mobility: A Review," *AIP Conference Proceedings*, Vol. 3016, 2024, p. 050001. https://doi.org/10.1063/5.0185525.

[3] Páscoa, J. C., Dumas, A., and Trancossi, M., "A Novel Look at the Performance of the Cyclorotor Propulsion System for Air Vehicles," *Proceedings of the ASME International Mechanical Engineering Congress and Exposition*, American Society of Mechanical Engineers, 2012, pp. 455–462. https://doi.org/10.1115/imece2012-85544.

[4] Halder, A., Kellen, A., and Benedict, M., "Aeroacoustic Analysis of UAV-Scale Cycloidal Rotor: An Experimental and Computational Approach," *Proceedings of the Vertical Flight Society 75th Annual Forum*, The Vertical Flight Society, 2019, pp. 1–20. https://doi.org/10.4050/f-0075-2019-14446.

[5] Krüger, T., Kusumaatmaja, H., Kuzmin, A., Shardt, O., Silva, G., and Viggen, E. M., *The Lattice Boltzmann Method: Principles and Practice*, Graduate Texts in Physics, Springer International Publishing, 2017. https://doi.org/10.1007/978-3-319-44649-3.

[6] Yakhot, V., and Orszag, S. A., "Renormalization Group Analysis of Turbulence. I. Basic Theory," *Journal of Scientific Computing*, Vol. 1, No. 1, 1986, pp. 3–51. https://doi.org/10.1007/bf01061452.

[7] Li, Y., "An Improved Volumetric LBM Boundary Approach and Its Extension for Sliding Mesh Simulation," Ph.D. thesis, Iowa State University, 2012. https://doi.org/10.31274/etd-180810-2467.

[8] Trascinelli, L., Romani, G., Hanson, L., Casalino, D., Zang, B., Zhou, B. Y., and Azarpeyvand, M., "Numerical Simulations of Large-Scale Turbulence Ingestion by a Forward Flight Propeller)," *The Journal of the Acoustical Society of America*, Vol. 158, No. 1, 2025, pp. 826–837. https://doi.org/10.1121/10.0037219.

[9] Grande, E., Shubham, S., Avallone, F., Ragni, D., and Casalino, D., "Computational Aeroacoustic Study of Co-Rotating Rotors in Hover," *Aerospace Science and Technology*, Vol. 153, 2024, p. 109381. https://doi.org/https://doi.org/10.1016/j.ast.2024.109381.

[10] Casalino, D., Romani, G., Pii, L. M., and Colombo, R., "Flow Confinement Effects on sUAS Rotor Noise," *Aerospace Science and Technology*, Vol. 143, 2023, p. 108756.

Downloaded by Technische Universiteit Delft on June 5, 2026 | http://arc.aiaa.org | DOI: 10.2514/6.2026-3447

[11] Casalino, D., Romani, G., Zhang, R., and Chen, H., "Lattice-Boltzmann Calculations of Rotor Aeroacoustics in Transitional Boundary Layer Regime," *Aerospace Science and Technology*, Vol. 130, No. 107953, 2022.

[12] Romani, G., Grande, E., Avallone, F., Ragni, D., and Casalino, D., "Computational Study of Flow Incidence Effects on the Aeroacoustics of Low blade-tip Mach Number Propellers," *Aerospace Science and Technology*, Vol. 120, 2022, p. 107275.

[13] Romani, G., Grande, E., Avallone, F., Ragni, D., and Casalino, D., "Performance and Noise Prediction of Low-Reynolds Number Propellers using the Lattice-Boltzmann Method," *Aerospace Science and Technology*, Vol. 125, 2021, p. 107086.

[14] Casalino, D., Grande, E., Romani, G., Ragni, D., and Avallone, F., "Definition of a Benchmark for Low Reynolds Number Propeller Aeroacoustics," *Aerospace Science and Technology*, Vol. 113, 2021.

[15] Verniere, F. D., Sticchi, E., Casalino, D., Ragni, D., and Zamponi, R., "Aeroacoustic Analysis of a Transitioning Vectored-Thrust/Tilt-Rotor UAM Vehicle Using the LB/VLES Method," *European Rotorcraft Forum 2025*, 2025.

[16] Casalino, D., van der Velden, W., and Romani, G., "Community Noise of Urban Air Transportation Vehicles," *AIAA Paper 2019-1834*, 2019.

[17] Casalino, D., van der Velden, W. C., Romani, G., and Gonzalez-Martino, I., "Aeroacoustic Analysis of Urban Air Operations Using the LB/VLES Method," *25th AIAA/CEAS Aeroacoustics Conference*, American Institute of Aeronautics and Astronautics, 2019. https://doi.org/10.2514/6.2019-2662.

[18] Williams, J. F., and Hawkings, D. L., "Sound Generation by Turbulence and Surfaces in Arbitrary Motion," *Philosophical Transactions for the Royal Society of London. Series A, Mathematical and Physical Sciences*, 1969, pp. 321–342.

[19] Mendez, S., Shoeybi, M., Lele, S. K., and Moin, P., "On the Use of the Ffowcs Williams-Hawkings Equation to Predict Far-Field Jet Noise from Large-Eddy Simulations," *International Journal of Aeroacoustics*, Vol. 12, No. 1–2, 2013, pp. 1–20. https://doi.org/10.1260/1475-472x.12.1-2.1.

[20] Heimerl, J., Benedict, M., and Halder, A., "Lichten Runner-Up Paper: Experimental and Computational Investigation of a UAV-Scale Cycloidal Rotor in Forward Flight," *Proceedings of the Vertical Flight Society 77th Annual Forum*, The Vertical Flight Society, 2021, pp. 1–18. https://doi.org/10.4050/f-0077-2021-16704.

[21] Benedict, M., Jarugumilli, T., and Chopra, I., "Experimental Optimization of MAV-Scale Cycloidal Rotor Performance," *Journal of the American Helicopter Society*, Vol. 56, No. 2, 2011, pp. 22005–22005.

[22] Litherland, B. L., Borer, N. K., and Zawodny, N. S., "X-57 Maxwell High-Lift Propeller Testing and Model Development," *AIAA AVIATION 2021 FORUM*, American Institute of Aeronautics and Astronautics, 2021, pp. 2021–3193. https://doi.org/10.2514/6.2021-3193.

[23] Goyal, J., Avallone, F., and Sinnige, T., "Isolated Propeller Aeroacoustics at Positive and Negative Thrust," *Aerospace Science and Technology*, Vol. 147, 2024, p. 109021. https://doi.org/10.1016/j.ast.2024.109021.

[24] Greenwood, E., and Schmitz, F. H., "Separation of Main and Tail Rotor Noise from Ground-Based Acoustic Measurements," *Journal of Aircraft*, Vol. 51, No. 2, 2014, pp. 464–472. https://doi.org/10.2514/1.c032046.

[25] Casalino, D., Barbarino, M., and Visingardi, A., "Simulation of Helicopter Community Noise in Complex Urban Geometry," *AIAA Journal*, Vol. 48, No. 8, 2011, pp. 1614–1624.

[26] Sinnige, T., "Aerodynamic and Aeroacoustic Interaction Effects for Tip-Mounted Propellers: An Experimental Study," Dissertation (tu delft), Delft University of Technology, 2018. https://doi.org/10.4233/uuid:214e1e9a-c53e-47c7-a12c-b1eb3ec8293b.

[27] Zarri, A., Koutsoukos, A., and Avallone, F., "Aerodynamic and Acoustic Interaction Effects of Adjacent Propellers in Forward Flight," *AIAA AVIATION 2023 Forum*, American Institute of Aeronautics and Astronautics, 2023. https://doi.org/10.2514/6.2023-4489.

Downloaded by Technische Universiteit Delft on June 5, 2026 | http://arc.aiaa.org | DOI: 10.2514/6.2026-3447